

Collective Neutrino Oscillations in Three Flavors on Qubit and Qutrit Processors

Luca Spagnoli,^{1,2} Noah Goss,^{3,4} Alessandro Roggero,^{1,2} Ermal Rrapaj,^{5,6,7} Michael J. Cervia,⁸ Amol V. Patwardhan,^{9,10} Ravi K. Naik,^{3,4} A. Baha Balantekin,¹¹ Ed Younis,⁴ David I. Santiago,^{3,4} Irfan Siddiqi,^{3,4} and Sheakha Aldaihan¹²

¹*Physics Department, University of Trento, Via Sommarive 14, I-38123 Trento, Italy*

²*INFN-TIFPA Trento Institute of Fundamental Physics and Applications, Trento, Italy*

³*Quantum Nanoelectronics Laboratory, Department of Physics, University of California at Berkeley, Berkeley, CA 94720, USA*

⁴*Applied Mathematics and Computational Research Division, Lawrence Berkeley National Laboratory, Berkeley, CA 94720, USA*

⁵*National Energy Research Scientific Computing Center, Lawrence Berkeley National Laboratory, Berkeley, CA 94720, USA*

⁶*Department of Physics, University of California, Berkeley, CA 94720, USA*

⁷*RIKEN iTHEMS, Wako, Saitama 351-0198, Japan*

⁸*Department of Physics, University of Washington, Seattle, WA 98195, USA*

⁹*School of Physics and Astronomy, University of Minnesota, Minneapolis, MN 55455, USA*

¹⁰*Department of Physics, New York Institute of Technology, New York, NY 10023, USA*

¹¹*Department of Physics, University of Wisconsin, Madison WI 53706, USA*

¹²*Department of Physics, Gettysburg College, Gettysburg, Pennsylvania 17325, United States*

Collective neutrino flavor oscillations are of primary importance in understanding the dynamic evolution of core-collapse supernovae and subsequent terrestrial detection, but also among the most challenging aspects of numerical simulations. This situation is complicated by the quantum many-body nature of the problem due to neutrino-neutrino interactions which demands a quantum treatment. An additional complication is the presence of three flavors, which often is approximated by the electron flavor and a heavy lepton flavor. In this work, we provide both qubit and qutrit encodings for all three flavors, and develop optimized quantum circuits for the time evolution and analyze the Trotter error. We conclude our study with a hardware experiment of a system of two neutrinos with superconducting hardware: the IBM Torino device for qubits and AQT device for qutrits. We find that error mitigation greatly helps in obtaining a signal consistent with simulations. While hardware results are comparable at this stage, we expect the qutrit setup to be more convenient for large-scale simulations since it does not suffer from probability leakage into nonphysical qubit space, unlike the qubit setup.

I. INTRODUCTION

Within the last several decades our knowledge of neutrino properties has grown significantly [1, 2]. However, even state-of-the-art three-dimensional hydrodynamical simulations of core-collapse supernova do not yet include the physics of neutrino flavor oscillations. Therefore, the precise extent to which these oscillations can affect the dynamics of this explosion and the accompanying nucleosynthesis remains an open question [3–5]. Indeed, flavor oscillations in such dense media are complex phenomena, because neutrinos not only interact with matter, yielding a one-body interaction term, but also with each other, introducing the two-body interaction term to a Hamiltonian that accounts for the collective neutrino oscillations (for reviews, see Refs. [6–12]). The latter contribution makes the neutrino flavor oscillations a manifestly dynamic many-body problem [13, 14].

There are roughly 10^{58} neutrinos emitted from a core-collapse supernova within 10s of seconds. Solving a quantum many-body problem for such a large number of particles is computationally formidable. To circumvent this hindrance, it is tempting to make approximations such as with a mean field treatment, in which a many-body problem is translated to an effective one-body problem.

The mean-field approximation is a powerful tool to tackle the problem and learn about the role of collective oscillations, but it comes at a cost of losing quantum entanglement, which can be measured in the form of quantum correlations and can even impact single body observables such as the flavor composition of the neutrinos detected from these events. To assess the validity of the mean-field approach, several simplified many-body models in a two-flavor framework have been explored [14–37] and differences have been found in the evolution of certain observables, compared to the corresponding mean-field predictions. For simple geometries, such as a two-beam setup with a constant neutrino gas density, one can efficiently perform computations with tensor network methods [25], but in more general settings with higher entanglement only a system of few tens of neutrinos could be simulated [31]. Aside from the challenges of adding more neutrinos, recent explorations have also sought to ask different questions—for instance, whether these deviations from the mean-field behavior could persist if the effects of finite interaction time [38, 39], non-forward scattering [40, 41], or Pauli blocking [42] are considered.

A more realistic treatment of this problem also warrants the inclusion of all three neutrino flavors in this formalism [43]. It has been observed from the mean-field

calculations that the three-flavor collective neutrino oscillations exhibit unique features like multiple spectral splits. From the many-body calculations in the three-flavor settings, it was found that the neutrinos are even more entangled than the two-flavor case, further questioning the reliability of the mean-field approximation in this realistic setting [44]. As shown in recent works, quantum magic (in essence a measure of the computational resources required for the simulation) as quantified by the stabilizer Renyi entropy can reach its maximal value in the dynamics of three-flavor collective oscillations [45]. However, such simulations were limited to only a few neutrinos due to the memory requirements for the large Hilbert space.

Quantum computers are presumably a natural choice to simulate the quantum many-body problems [46–48]. Several efforts have been made to simulate collective neutrino oscillations on a quantum computer in the two-flavor setting [49–54] and, more recently, also with the full three flavors [55, 56]. Here, we seek to develop optimized circuits for both qubit and qutrit representations based upon the specific properties of the Hamiltonian and the two-body interactions. In Sec. II we represent the Hamiltonian and the resulting SU(3) flavor algebra properties, irrespective of encoding. Then, we proceed to analyze the Trotter error in Sec. III and outline the qubit and qutrit representations of our model in Sec. IV.

We optimize the resulting quantum circuits in Sec. V. In Sec. VI we apply the computed circuits to study a system of two neutrinos on the IBM Torino superconducting quantum computing device for the qubit setup, and on the AQT device for the qutrit setup. Finally, we summarize and remark upon findings and future outlook in Sec. VII.

II. ALGEBRA OF COLLECTIVE THREE-FLAVOR OSCILLATIONS

Here, we introduce the Hamiltonian model for collective neutrino oscillations in three flavors. Accounting only for forward scattering, the Hamiltonian governing the flavor evolution for a system of N neutrinos can be expressed as $H = H_\nu + H_{\nu\nu}$, where H_ν encompasses the one-body neutrino interaction terms, including vacuum oscillations and interactions with the matter background. The full two-body term including momentum exchanges [41] is beyond the scope of this article and will be treated in future work.

Ignoring neutrino-matter interactions for simplicity (as they can be nearly rotated away with an appropriate change-of-basis transformation), the contribution from vacuum oscillations can be written as

$$H_\nu = \sum_{q=1}^N \omega_q \vec{B} \cdot \vec{\lambda}_q. \quad (1)$$

Within the Hilbert subspace of each neutrino indexed by q , we denote by $\vec{\lambda}$ the vector of Gell-Mann matrices, and

\vec{B} is likewise a constant, eight-component unit vector. Defining the neutrino mass-squared differences, $\Delta_{ij} = m_i^2 - m_j^2$, we express the vacuum oscillation frequencies ω_q and the non-zero entries of \vec{B} in the mass basis as follows:

$$\begin{aligned} \omega_q &= \frac{\sqrt{\Delta_{12}^2 + (\Delta_{13} + \Delta_{23})^2/3}}{4p_q} \\ B_3 &= \frac{\Delta_{12}}{\sqrt{\Delta_{12}^2 + (\Delta_{13} + \Delta_{23})^2/3}} \\ B_8 &= \frac{\Delta_{13} + \Delta_{23}}{\sqrt{3\Delta_{12}^2 + (\Delta_{13} + \Delta_{23})^2}}. \end{aligned} \quad (2)$$

All other elements of \vec{B} are zero.

Similarly, we may write the two-body term

$$H_{\nu\nu} = \frac{\mu}{2N} \sum_{q<k}^N (1 - \cos(\theta_{qk})) \vec{\lambda}_q \cdot \vec{\lambda}_k := \sum_{q<k}^N J_{qk} \vec{\lambda}_q \cdot \vec{\lambda}_k, \quad (3)$$

where coupling constant $\mu = \sqrt{2}G_F n_\nu$ depends on both Fermi's constant G_F and the local neutrino number density n_ν ($= N/V$ for N neutrinos quantized in a box of volume V). A full derivation of the Hamiltonian can be found in Appendix A.

The Gell-Mann matrices satisfy the following algebra,

$$\begin{aligned} [\lambda_i, \lambda_j] &= 2if_{ijk}\lambda_k, \\ f^{147} &= -f^{156} = f^{246} = f^{257} = f^{345} = -f^{367} = \frac{1}{2} \\ f^{458} &= f^{678} = \frac{\sqrt{3}}{2}, \quad f^{123} = 1 \end{aligned} \quad (4)$$

We note that there are three embedded SU(2) subalgebras,

$$\begin{aligned} i &\rightarrow \{\lambda_1, \lambda_2, \lambda_3\} \\ j &\rightarrow \{\lambda_4, \lambda_5, \lambda_+\} \\ k &\rightarrow \{\lambda_6, \lambda_7, \lambda_-\}, \end{aligned} \quad (5)$$

where $\lambda_\pm = \frac{1}{2}(\pm\lambda_3 + \sqrt{3}\lambda_8)$ and have denoted them by (i, j, k) . The Casimir operators $(\vec{\lambda} \cdot \vec{\lambda})_{i,j,k}$ of these subalgebras mutually commute. Another important property of the SU(n) quadratic Casimir operator is its relation to the SWAP operator,

$$\frac{1}{n}\mathbb{1}_n + \frac{1}{2}\vec{g}_q \cdot \vec{g}_k = \text{SWAP}_{qk}, \quad (6)$$

where $\text{SWAP}|x\rangle|y\rangle = |y\rangle|x\rangle$ for any pair vectors in the respective n -dimensional qudit spaces, and \vec{g} are the generators of the algebra, i.e., Pauli matrices for SU(2) and Gell-Mann matrices for SU(3).

III. TROTTER ERROR

Given the Hamiltonian model for oscillations outlined in the previous section, we are ready to describe how

we simulate real-time evolution of a neutrino system. In order to implement the time evolution operator e^{-iHt} we will use a simple Trotterization method.

First, we can approximate the evolution operator by breaking it into the product of the vacuum interaction and the 2-body term as follows:

$$e^{-iHt} \approx e^{-iH_\nu t} e^{-iH_{\nu\nu} t} \quad (7)$$

and the error in doing this approximation is [57]

$$\|e^{-iHt} - e^{-iH_\nu t} e^{-iH_{\nu\nu} t}\| \leq \frac{t^2}{2} \|[H_\nu, H_{\nu\nu}]\|. \quad (8)$$

More precisely, in Appendix B we calculate the bound

$$\|e^{-iHt} - e^{-iH_\nu t} e^{-iH_{\nu\nu} t}\| \leq t^2 \mu N \max_{q,k} |\omega_k - \omega_q|. \quad (9)$$

The one-body term H_ν is itself a sum of commuting single-body operators, so we may simply factor

$$e^{-iH_\nu t} = \prod_{q=1}^N e^{-it\omega_q \vec{B} \cdot \vec{\lambda}_q}, \quad (10)$$

without involving any further approximation. Moreover, for the two-body interaction, we can use again the first order Trotter formula, factoring individual interaction terms;

$$\begin{aligned} & \left\| e^{iH_{\nu\nu} t} - \prod_{q < k} e^{-itJ_{qk} \vec{\lambda}_q \cdot \vec{\lambda}_k} \right\| \leq \\ & \frac{t^2}{2} \sum_{K=1}^{\binom{N}{2}} J_K \left\| \left[\vec{\lambda}_{q_K} \cdot \vec{\lambda}_{k_K}, \sum_{L > K} \vec{\lambda}_{q_L} \cdot \vec{\lambda}_{k_L} \right] \right\| =: \frac{t^2}{2} \|C_{22}\| \end{aligned} \quad (11)$$

where J_K is the coupling strength for the pair $K = 1, \dots, \binom{N}{2}$. As shown in detail in the full derivation presented in Appendix B we have

$$\|C_{22}\| < \sqrt{3} \mu^2 N \max_{q,k,l} |\cos(\theta_{lq}) - \cos(\theta_{lk})|. \quad (12)$$

In general, by doing r steps with time t/r , the full Trotter error will be bounded by

$$\frac{t^2}{2r} (2\mu N \max_{q,k} |\omega_k - \omega_q| + \|C_{22}\|). \quad (13)$$

By increasing the number of steps r , and thus the number of operations, we can reduce the approximation error.

Notably, our above analysis is independent of the representation of neutrino flavor on hardware, applying equally well to simulations on qubit and qutrit hardware.

IV. QUTRIT AND QUBIT REPRESENTATIONS

Having outlined the Hamiltonian for collective oscillations and how to decompose the evolution operator into its individual terms, it remains to be shown how they are simulated on quantum hardware. Before showing the operations on qubits or qutrits to simulate our system, let us introduce how to encode our problem on each kind of hardware.

When considering qutrit-based hardware, we can straightforwardly encode each neutrino with a single qutrit, by associating each flavor of a neutrino with a different state of the qutrit. Our convention is as follows:

$$|\nu_e\rangle = |0\rangle, \quad |\nu_\mu\rangle = |1\rangle, \quad |\nu_\tau\rangle = |2\rangle. \quad (14)$$

This encoding is particularly easy to use, since it preserves the locality of the Hamiltonian: one-body terms become single-qutrit gates, and two-body terms become two-qutrit gates. Consequently, the depth and gate count will be much lower here than in the qubit case.

Next, we explain the mapping from neutrinos onto qubits. A three-flavor neutrino has three possible states, which means that we need two qubits for each neutrino, entailing one extra ‘unphysical’ state, which ideally will never be used. Considering the computational basis of two qubits, we choose the following encoding:

$$\begin{aligned} |\nu_e\rangle &= |01\rangle, \quad |\nu_\mu\rangle = |10\rangle \\ |\nu_\tau\rangle &= |11\rangle, \quad |\tilde{\nu}\rangle = |00\rangle \end{aligned} \quad (15)$$

Since the state $|\tilde{\nu}\rangle$ is non-physical, no wave-function amplitude should propagate into this state throughout the entire time evolution.

Likewise, we map the generators of the SU(3) algebra, the Gell-Mann matrices that we denoted with $\vec{\lambda}$ above, into a two-qubit operator space spanned by Pauli strings of the form $\{\sigma_i \otimes \sigma_j\}_{i,j=0,1,2,3}$. Note that this mapping must be consistent with the mapping of states above, so that the new two-qubit operators reduce correctly to the Gell-Mann matrices if we delete the $|00\rangle$ state. This mapping is given by the following definitions,

$$\begin{aligned} 2Q_1 &= X_0 X_1 + Y_0 Y_1 & 2Q_2 &= Y_0 X_1 - X_0 Y_1 \\ 2Q_3 &= Z_0 \mathbb{1}_1 - \mathbb{1}_0 Z_1 & 2Q_4 &= X_0 \mathbb{1}_1 - X_0 Z_1 \\ 2Q_5 &= Y_0 \mathbb{1}_1 - Y_0 Z_1 & 2Q_6 &= \mathbb{1}_0 X_1 - Z_0 X_1 \\ 2Q_7 &= \mathbb{1}_0 Y_1 - Z_0 Y_1 \\ 2Q_8 &= \frac{\mathbb{1}_0 Z_1 + Z_0 \mathbb{1}_1 - 2Z_0 Z_1}{\sqrt{3}}. \end{aligned} \quad (16)$$

Here we denote the 2×2 identity by $\mathbb{1}$ and the Pauli matrices $X, Y, Z = \sigma_{\{x,y,z\}}$. The subscript on the Pauli operators denotes the qubit on which operator acts, and we omitted the tensor product for brevity. In short, we have $Q_i = 0 \oplus \lambda_i$ (there the 0 entry is meant to be on the $|00\rangle \langle 00|$ entry of the matrix). With this definition, the Q_i matrices satisfy the same algebra of the Gell-Mann matrices. Thus we encode the SU(3) algebra

in a larger two-qubit space containing the non-physical $|\bar{\nu}\rangle$ state. The qubit-encoded Hamiltonian behaves in the same way as the original one in the subspace generated by $\{|01\rangle, |10\rangle, |11\rangle\}$ and does not involve the non-physical $|00\rangle$ state.

V. HARDWARE IMPLEMENTATION

We describe now the quantum circuit implementation of the time evolution operator, providing versions for both an all-to-all and a nearest-neighbors connectivity in the qubit case.

A. Qubit Circuit

Since we want to observe the flavor oscillations of neutrinos, we would like to encode and measure neutrinos in the flavor basis. However, the Hamiltonian is more concisely expressed in the mass basis, so we start our quantum circuit computations in the flavor basis, transform to the mass basis through the Pontecorvo-Maki-Nakagawa-Sakata (PMNS) matrix, apply time evolution, and finally transform back to the flavor basis before performing measurements. To be able to switch from one basis to the other we need to implement the PMNS matrix as a gate. This is a two-qubit gate that directly depends on the mixing angles, as explained in Appendix C 1, where we also provide its circuit. Our results are similar to those found in Ref. [58], which used a different qubit mapping for the three flavors, and we also provide a version in terms of cross resonance gates. Having computed the error associated with the Trotter approximation, here we focus on the gate implementation of the unitary operations $e^{-it\omega_q \vec{B} \cdot \vec{Q}_q}$ and $e^{-itJ_{qk} \vec{Q}_q \cdot \vec{Q}_k}$.

The exponent of the one-body term can be written as a linear combination of Z_0, Z_1 and $Z_0 Z_1$, which are mutually commuting operators. As demonstrated in Appendix C 2, in the physical subspace the unitary operator is equivalent to a product of single qubit rotations $R_{Z_0}(\alpha)R_{Z_1}(\beta)$ up to a global phase, for an appropriate choice of the angles α and β . We can then implement the evolution under the one-body term without using entangling operations, a strategy also employed recently in Ref. [55].

Using the commutation relations given by the subalgebras in Eq. (5), one finds that $\vec{Q}_q \cdot \vec{Q}_k$ can be broken into the following commuting pieces (denoting $Q_i \otimes Q_i = Q_{ii}$):

$$\begin{aligned} \sum_i Q_{ii} &= (Q_{11} + Q_{22}) + (Q_{44} + Q_{55}) \\ &+ (Q_{66} + Q_{77}) + (Q_{33}) + (Q_{88}) \end{aligned} \quad (17)$$

where each parenthetical term commutes with every other. Therefore we can break the exponential *exactly*,

as follows:

$$\begin{aligned} e^{-itJ_{qk} \vec{Q}_q \cdot \vec{Q}_k} &= e^{-itJ_{qk}(Q_{11}+Q_{22})_{qk}} \times \\ &e^{-itJ_{qk}(Q_{44}+Q_{55})_{qk}} \times \\ &e^{-itJ_{qk}(Q_{66}+Q_{77})_{qk}} \times \\ &e^{-itJ_{qk}(Q_{33})_{qk}} e^{-itJ_{qk}(Q_{88})_{qk}}, \end{aligned} \quad (18)$$

where we used the subscript qk in the parenthesis surrounding the operator to clarify on which qubits the operators actually act. For instance with the notation $(Q_{33})_{qk}$ we intend the tensor product between Q_3 acting on the pair of qubits representing neutrino k and Q_3 on the pair for neutrino q .

Now, for example let us consider in detail the second exponential $e^{-itJ_{qk}(Q_{44}+Q_{55})_{qk}}$. We can write $Q_{44}+Q_{55}$ in terms of Pauli matrices using the mapping from Eq. (16)

$$\begin{aligned} Q_4 \otimes Q_4 &= \frac{X_1 X_3}{4} (1 - Z_4 - Z_2 + Z_2 Z_4), \\ Q_5 \otimes Q_5 &= \frac{Y_1 Y_3}{4} (1 - Z_4 - Z_2 + Z_2 Z_4). \end{aligned} \quad (19)$$

Then, we define the following operator:

$$\begin{array}{c} q_a \\ q_b \end{array} \begin{array}{|c|} \hline G_{ab} \\ \hline \end{array} := \begin{array}{c} \boxed{H} \\ \bullet \\ \text{---} \\ \oplus \end{array} \quad (20)$$

It is straightforward to prove that G_{13} diagonalizes the operator $Q_{44} + Q_{55}$ (see Appendix C 4 for details), and thus

$$G_{13} (Q_{44} + Q_{55}) G_{13}^\dagger = \frac{Z_1 - Z_1 Z_3}{4} \times (1 - Z_4 - Z_2 + Z_2 Z_4) \quad (21)$$

Using this unitary transformation, the exponential term $e^{-itJ_{qk}(Q_{44}+Q_{55})_{qk}}$ can then be implemented as,

$$G_{13}^\dagger e^{-itJ_{qk} \left(\frac{Z_1 - Z_1 Z_3}{4} (1 - Z_4 - Z_2 + Z_2 Z_4) \right)_{qk}} G_{13}. \quad (22)$$

We can implement $e^{-itJ_{qk}(Q_{66}+Q_{77})_{qk}}$ and $e^{-itJ_{qk}(Q_{11}+Q_{22})_{qk}}$ in a similar fashion. The diagonal unitary operations $e^{-itJ_{qk}Q_{33}}$ and $e^{-itJ_{qk}Q_{88}}$ are four-qubit operators whose weight can be reduced by introducing gadgets similar to the diagonalizing operator G_{ab} . Implementation details (i.e., in terms of elementary gates) for all these terms can be found in Appendices C 3 and C 4. Our circuit implementation requires 34 CNOT gates when qubits have all-to-all connectivity and 39 CNOT gates for the T connectivity present on IBM devices. It is likely that further optimization could be done since the authors of Ref. [55] obtain circuits with only 18 CNOT with all-to-all connectivity and 30 CNOT for qubits on a chain, even though the mapping of the flavor space is slightly different from ours.

B. Qutrit circuit

By considering qutrits instead of qubits, each neutrino can be encoded with a single qutrit. The PMNS matrix is then a single-qutrit gate, which is in general easy to implement, as are the single-body Hamiltonian terms. So, in the following we will only focus on the two-body term, which requires the use of two-qutrit gates.

Let us introduce the $C\tilde{X}$ gate, introduced in Ref. [59], defined as follows:

$$C\tilde{X} |x\rangle |y\rangle = |x\rangle |-x-y\rangle \quad (23)$$

This gate is self-inverse and can be decomposed into three two-level controlled gates as

$$\quad (24)$$

It can be implemented with a qutrit controlled- Z gate (defined as $CZ_3 = \sum_{k,l \in \mathbb{Z}_3} \omega^{kl} |kl\rangle \langle kl|$, where $\omega = e^{2\pi i/3}$ is the third root of unity) and a single-qutrit quantum Fourier transform, which is nothing but the generalization of the Hadamard gate. By using this gate, the two-qutrit SWAP becomes the standard circuit if we replace the CNOTs with $C\tilde{X}$:

$$\text{SWAP} = \quad (25)$$

Since we need a partial swap to simulate the interaction, we can generalize the procedure of qubits, and replace the middle CX with a CR . Here, CR is a controlled- $SU(3)$ gate where the $SU(3)$ operation is the product of a two-level phase gate P_z gate and a two-level rotation R_x gate,

$$\begin{aligned} R^{12}(\theta) &= \begin{pmatrix} e^{-i\theta} & 0 & 0 \\ 0 & \cos(\theta) & -i \sin(\theta) \\ 0 & -i \sin(\theta) & \cos(\theta) \end{pmatrix} \\ &= P_z^{01}(\theta) R_x^{12}(\theta) \\ R^{02}(\theta) &= P_z^{12}(\theta) R_x^{02}(\theta) \\ R^{01}(\theta) &= P_z^{21}(\theta) R_x^{01}(\theta) \end{aligned} \quad (26)$$

The resulting circuit, which applies $e^{-2i\theta \text{SWAP}}$, is:

$$\quad (27)$$

Given this quantum circuit, there are many ways one can implement it on hardware. We use a compiler to optimize the quantum circuit in terms of CZ_3 gates and single-qutrit rotations. By leveraging our compiler with a numerical synthesis tolerance of 10^{-6} (significantly lower than any gate infidelities on the device), we construct

circuits that require four CZ_3 gates plus local $SU(3)$ rotations per Trotter step. Our $SU(3)$ rotations were implemented by embedded $SU(2)$ rotations with subspace Rabi oscillations [60, 61]. We note that the gate cost of our qutrit circuit is the same as the corresponding construction from Ref. [55].

VI. HARDWARE EXPERIMENTS

We can now proceed to study the circuits developed in the previous section on the IBM Torino device and the AQT qutrit device. The AQT qutrit device is a Transmon-based quantum processor designed and operated to perform qudit operations and implement arbitrary single qudit gates and multi-qudit gates such as CZ_3 [62–64]. Based on the past success with similar algorithms, we implement an error mitigation technique based on noise renormalization [65–68]. We first apply Pauli twirling to the compiled circuits in order to approximate the error channel of the device as global depolarizing noise

$$\Lambda[\rho] = (1-p)\rho + \frac{p}{\text{Tr}[\mathbb{1}]} \mathbb{1}, \quad (28)$$

with $\mathbb{1}$ the global identity matrix, ρ the noiseless quantum state and p the noise strength [69, 70]. Strictly speaking, Pauli twirling does not convert a generic quantum channel into a depolarizing channel, but into a stochastic Pauli channel, which in practice may be approximated by the depolarizing channel rather well.

We perform simulations of the time-evolution using the first-order product formula from Eq. (7) with a fixed time-step $dt = 0.5\mu^{-1}$. With this strategy to reach a total evolution time $t = Ldt$, we need to perform L layers of single steps involving evolution with both the one-body and two-body Hamiltonians. Since we expect the noise strength to depend on the circuit depth, we expect to have the following noisy state

$$\Lambda[\rho(t = Ldt)] = (1-p_L)\rho(t = Ldt) + \frac{p_L}{\text{Tr}[\mathbb{1}]} \mathbb{1}, \quad (29)$$

with $p_L \rightarrow 1$ as $L \rightarrow \infty$. We estimate p_L , for a given depth, using a calibration circuit involving only Clifford gates and use the results to remove the error contribution. The Clifford circuit has the same gate structure as the target circuit, but performs a SWAP operation by leveraging Eq. (6). For instance, if we are interested in expectation values $\langle \Pi_k(t) \rangle$ of some projector operator Π_k at time $t = Ldt$, we can use the calibration circuit to get

$$\langle \Pi_c(L) \rangle_{\text{calib}} = (1-p_L) + \frac{p_L}{\text{Tr}[\mathbb{1}]}, \quad (30)$$

where Π_c is a rank-1 projector on the state we expect to observe in the absence of noise. The resulting expectation value can be used to determine empirically the circuit fidelity as a function of depth. The results for two three-flavor neutrinos on both devices is shown in Fig. 1.

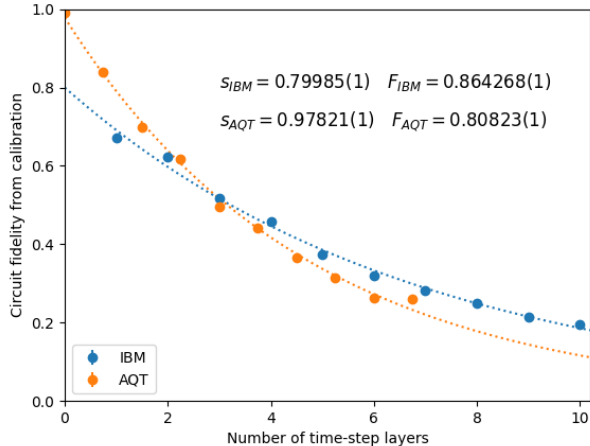


FIG. 1. Fidelity normalization factor estimation by Clifford version of the circuit assuming depolarizing noise. Blue dotted points depict results from the IBM device, and orange points from the AQT device. The curves plotted are fits of the aforementioned data to an exponential function, as in Eq. (31). In the plot we show uncertainties by including the standard error with vertical lines, which are rather small. Since the AQT device used three CZ gates for calibration and four CZ gates for time evolution, the time steps have been rescaled by a factor of $3/4$. For $t = 0$ we show the initial state preparation results for both devices. As state preparation in the qubit case requires entangling gates, SPAM error is higher than the qutrit case.

Further, we model the results obtained with an exponential fit of the form

$$\langle \Pi_c(L) \rangle_{calib} = sF^L, \quad (31)$$

where the base F represents a fidelity per step and the coefficient s accounts for state-preparation and measurement (SPAM) errors. The best fit parameters for both devices are reported inside the plot in Fig. (1). The much larger SPAM error observed in the qubit case—even when no time-steps are performed (ie. $L = 0$)—is in large part a consequence of the transformations between the flavor and mass bases, which involve entangling operations. In contrast, on the qutrit implementation, state preparation involves only local $SU(3)$ transformations instead.

The error mitigation proceeds then as follows: we first estimate the depolarizing noise strength p_L using Eq. (30) obtaining

$$p_L = \frac{\text{Tr}[\mathbb{1}]}{\text{Tr}[\mathbb{1}] - 1} (1 - \langle \Pi_c(L) \rangle_{calib}). \quad (32)$$

For the qubit simulations we estimate $\langle \Pi_c(L) \rangle_{calib}$ directly from the measured calibration circuits. For the qutrit case, owing to the difference in gate counts per layer between the simulation circuits and the calibration ones, we use instead the fit from Eq. (31) which provides

a good model for the measured data. Using this estimator for the noise strength we can then estimate the noise mitigated expectation value of a rank-1 projector Π_k as follows

$$\langle \Pi_k(L) \rangle_{mit} = \frac{\langle \Pi_k(L) \rangle - \frac{p_L}{\text{Tr}[\mathbb{1}]}}{1 - p_L}. \quad (33)$$

In the qubit case we can express the mitigated expectation value directly in terms of the bare expectation value and the result of calibration at step L as

$$\langle \Pi_k(L) \rangle_{mit} = \frac{15 \langle \Pi_k(L) \rangle + \langle \Pi_c(L) \rangle_{calib} - 1}{16 \langle \Pi_c(L) \rangle_{calib} - 1}, \quad (34)$$

where we used $\text{Tr}[\mathbb{1}] = 16$ for our four qubits. We have checked that the mitigated values obtained from the fit in the qubit case agree quite well with the extrapolation from the bare Clifford circuits.

We present a selection of results from our simulations in Fig. 2. A complete set of results is provided in the Appendix D. The system is initially prepared in the state $|\nu_e \nu_\mu\rangle$ and evolved under the full flavor Hamiltonian $H = H_\nu + H_{\nu\nu}$ using a first order Trotter formula as discussed in Sec. III. The neutrino frequencies are $\omega = \{2, 2.5\} \mu^{-1}$. The mass dependent parameters are $\{B_3, B_8\} = \{0.025483, 0.999567\}$. The mixing angles are $\theta_{12} = 33.44^\circ$, $\theta_{13} = 8.57^\circ$, $\theta_{23} = 49.2^\circ$, $\delta_{cp} = 0$. Here we show the survival probabilities of $|\nu_e \nu_\mu\rangle$ and $|\nu_\mu \nu_e\rangle$ evolved for up to ten time steps, before and after performing error mitigation techniques described earlier. We can observe that bare results do not match expected theoretical values beyond the first couple of Trotter steps, and as time increases resembles an equipartition of probabilities among all states. The match to the theoretical results at later times is more likely coincidence. Mitigation improves results rather drastically, with both devices agreeing with theoretical expectations for up to five Trotter steps, particularly for the flavor probability of the $|\nu_\mu \nu_e\rangle$ state, which is very small throughout the time evolution and therefore more challenging to resolve.

VII. CONCLUSION AND DISCUSSION

In this work, we have developed and compared quantum circuits to perform collective neutrino flavor oscillations on both qubit and qutrit quantum hardware. Time evolution was computed through the first-order Trotter approximation and we find that, for a fixed total time, the error scales linearly with the number of neutrinos and inversely with the number of Trotter steps. In the qubit encoding, the one-body term becomes a two-qubit operator as does the PMNS matrix, and as such even initial product state preparation requires entangling gates. Meanwhile, in the qutrit case no such need arises. For noisy, intermediate-scale quantum (NISQ) hardware, this translates to additional noise for state preparation on

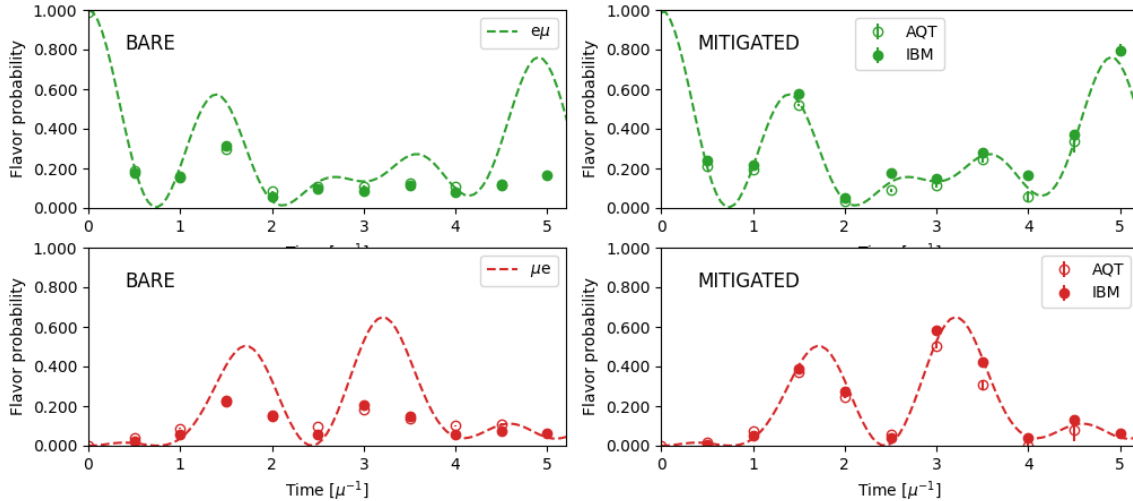


FIG. 2. Survival probability for the initial state $|\nu_e\nu_\mu\rangle$ (top) and its swapped counterpart $|\nu_\mu\nu_e\rangle$ (bottom) as function of time evolution. We show the results from measurements both directly on the device (left) and after error mitigation (right) for up to ten time steps. Solid dots are the results from the (qubit-based) IBM Torino device and empty dots are the results from the (qutrit-based) AQT device. Uncertainty bars are estimated by the standard error from each simulation on hardware. Exact results are plotted as curves for reference. The improvement due to error mitigation is quite drastic, and depolarizing noise, after Pauli twirling has been performed, seems to be a significant fraction of the noise.

qubits. Similarly, the time evolution will have more entangling gates for the qubit setup, as two-body interactions become four-qubit gates, which are decomposed into a sequence of one- and two-qubit gates. Even with the optimized circuits we construct through various gadgets (see Sec. IV and Appendix C), there is significant overhead for a neutrino pair time evolution step. For both hardware, in larger systems, SWAP operations will be required to represent the all-to-all two-body interactions, which fortunately we can absorb in the two-body operation due to Eq. (6). On the other hand, qutrit gates require higher control capabilities and can be prone to higher infidelities as a result. For both setups we need to perform error mitigation on hardware to achieve the quality of results shown in Fig. 2. We note that there are still large margins of improvement for fidelity of qutrit gates, and it is remarkable to see the level of control on these more complex architectures. Limited hardware connectivity issues will start to play an important role for larger systems, so the qutrit-based design is expected to have advantages in terms of overall fidelity.

One main difference between the two encodings is the mapping of the physical Hilbert space to the qudit space on device. In the case of qubits, there is one neutrino to two qubits, with one of the amplitudes being non-physical and decoupled from the rest during simulations. We take advantage of this fact to further improve our circuits and reduce the gate count. For a system of N neutrinos, the fraction of nonphysical states on the qubit device is $1 - (3/4)^N$, which becomes the vast majority of states as the number of particles increases. The presence of depo-

larizing noise will inevitably result in leakage to the non-physical space. On the qutrit device there is a one-to-one mapping between physical amplitudes and device amplitudes. Thus, despite the presence of noise, such leakage cannot occur. In supernovae simulations, the main observables are single-neutrino flavor measurements, and the overall flavor composition might be robust against leakage. However, correlations and higher order operators might be more sensitive to this type of noise. One could take into consideration hardware noise in devising encodings with noise-resistant observables, provided the noise is well-categorized. For now, we leave such endeavors for future research.

ACKNOWLEDGMENTS

We thank Alessandro Baroni and Pooja Siwach for the useful discussions. This research was supported in part by the U.S. Department of Energy, Office of Science, Office of High Energy Physics, under Award Nos. DE-SC0019465 and DE-SC0021143 and in part by the U.S. National Science Foundation Grants Nos. PHY-2020275 and PHY-2411495 at the University of Wisconsin. This work is part of the activities of the Quantum Computing for High-Energy Physics (QC4HEP) working group. This research used resources of the Oak Ridge Leadership Computing Facility, which is a DOE Office of Science User Facility supported under Contract DE-AC05-00OR22725. MJC is supported by the U.S. Department of Energy Grant No. DE-FG02-97ER-41014

(UW Nuclear Theory). AVP was supported by the U.S.

Department of Energy (DOE) under grant DE-FG02-87ER40328 at the University of Minnesota.

-
- [1] A. Baha Balantekin and B. Kayser, On the Properties of Neutrinos, *Ann. Rev. Nucl. Part. Sci.* **68**, 313 (2018).
- [2] P. Huber *et al.*, Snowmass Neutrino Frontier Report, in *Snowmass 2021* (2022) [arXiv:2211.08641](https://arxiv.org/abs/2211.08641) [hep-ex].
- [3] A. Mirizzi, I. Tamborra, H.-T. Janka, N. Saviano, K. Scholberg, R. Bollig, L. Hudepohl, and S. Chakraborty, Supernova Neutrinos: Production, Oscillations and Detection, *Riv. Nuovo Cim.* **39**, 1 (2016).
- [4] H.-T. Janka, Neutrino emission from supernovae, in *Handbook of Supernovae*, edited by A. W. Alsabti and P. Murdin (Springer International Publishing, Cham, 2017) pp. 1575–1604, [arXiv:1702.08713](https://arxiv.org/abs/1702.08713) [astro-ph.HE].
- [5] A. Burrows and D. Vartanyan, Core-Collapse Supernova Explosion Theory, *Nature* **589**, 29 (2021).
- [6] H. Duan, G. M. Fuller, and Y.-Z. Qian, Collective Neutrino Oscillations, *Ann. Rev. Nucl. Part. Sci.* **60**, 569 (2010).
- [7] S. Chakraborty, R. Hansen, I. Izaguirre, and G. Raffelt, Collective neutrino flavor conversion: Recent developments, *Nucl. Phys. B* **908**, 366 (2016).
- [8] A. B. Balantekin, Symmetries and Algebraic Methods in Neutrino Physics, *J. Phys. G* **45**, 113001 (2018).
- [9] I. Tamborra and S. Shalgar, New Developments in Flavor Evolution of a Dense Neutrino Gas, *Ann. Rev. Nucl. Part. Sci.* **71**, 165 (2021).
- [10] S. Richers and M. Sen, Fast Flavor Transformations, in *Handbook of Nuclear Physics*, edited by I. Tanihata, H. Toki, and T. Kajino (2022) pp. 1–17.
- [11] A. B. Balantekin, M. J. Cervia, A. V. Patwardhan, E. Rrapaj, and P. Siwach, Quantum information and quantum simulation of neutrino physics, *Eur. Phys. J. A* **59**, 186 (2023).
- [12] M. C. Volpe, Neutrinos from dense environments: Flavor mechanisms, theoretical approaches, observations, and new directions, *Rev. Mod. Phys.* **96**, 025004 (2024).
- [13] J. Pantaleone, Neutrino oscillations at high densities, *Physics Letters B* **287**, 128 (1992).
- [14] A. B. Balantekin and Y. Pehlivan, Neutrino-Neutrino Interactions and Flavor Mixing in Dense Matter, *J. Phys. G* **34**, 47 (2007).
- [15] N. F. Bell, A. A. Rawlinson, and R. F. Sawyer, Speedup through entanglement: Many body effects in neutrino processes, *Phys. Lett. B* **573**, 86 (2003).
- [16] A. Friedland and C. Lunardini, Neutrino flavor conversion in a neutrino background: Single particle versus multiparticle description, *Phys. Rev. D* **68**, 013007 (2003).
- [17] A. Friedland and C. Lunardini, Do many particle neutrino interactions cause a novel coherent effect?, *JHEP* **10**, 043.
- [18] A. Friedland, B. H. J. McKellar, and I. Okuniewicz, Construction and analysis of a simplified many-body neutrino model, *Phys. Rev. D* **73**, 093002 (2006).
- [19] B. H. J. McKellar, I. Okuniewicz, and J. Quach, Non-Boltzmann behaviour in models of interacting neutrinos, *Phys. Rev. D* **80**, 013011 (2009).
- [20] Y. Pehlivan, A. B. Balantekin, T. Kajino, and T. Yoshida, Invariants of Collective Neutrino Oscillations, *Phys. Rev. D* **84**, 065008 (2011).
- [21] S. Birol, Y. Pehlivan, A. B. Balantekin, and T. Kajino, Neutrino Spectral Split in the Exact Many Body Formalism, *Phys. Rev. D* **98**, 083002 (2018).
- [22] A. V. Patwardhan, M. J. Cervia, and A. Baha Balantekin, Eigenvalues and eigenstates of the many-body collective neutrino oscillation problem, *Phys. Rev. D* **99**, 123013 (2019).
- [23] M. J. Cervia, A. V. Patwardhan, A. B. Balantekin, t. S. N. Coppersmith, and C. W. Johnson, Entanglement and collective flavor oscillations in a dense neutrino gas, *Phys. Rev. D* **100**, 083001 (2019).
- [24] E. Rrapaj, Exact solution of multiangle quantum many-body collective neutrino-flavor oscillations, *Phys. Rev. C* **101**, 065805 (2020).
- [25] A. Roggero, Entanglement and many-body effects in collective neutrino oscillations, *Phys. Rev. D* **104**, 103016 (2021).
- [26] A. Roggero, Dynamical phase transitions in models of collective neutrino oscillations, *Phys. Rev. D* **104**, 123023 (2021).
- [27] Z. Xiong, Many-body effects of collective neutrino oscillations, *Phys. Rev. D* **105**, 103002 (2022).
- [28] J. D. Martin, A. Roggero, H. Duan, J. Carlson, and V. Cirigliano, Classical and quantum evolution in a simple coherent neutrino problem, *Phys. Rev. D* **105**, 083020 (2022).
- [29] A. V. Patwardhan, M. J. Cervia, and A. B. Balantekin, Spectral splits and entanglement entropy in collective neutrino oscillations, *Phys. Rev. D* **104**, 123035 (2021).
- [30] A. Roggero, E. Rrapaj, and Z. Xiong, Entanglement and correlations in fast collective neutrino flavor oscillations, *Phys. Rev. D* **106**, 043022 (2022).
- [31] M. J. Cervia, P. Siwach, A. V. Patwardhan, A. B. Balantekin, S. N. Coppersmith, and C. W. Johnson, Collective neutrino oscillations with tensor networks using a time-dependent variational principle, *Phys. Rev. D* **105**, 123025 (2022).
- [32] M. Illa and M. J. Savage, Multi-Neutrino Entanglement and Correlations in Dense Neutrino Systems, *Phys. Rev. Lett.* **130**, 221003 (2023).
- [33] D. Lacroix, A. B. Balantekin, M. J. Cervia, A. V. Patwardhan, and P. Siwach, Role of non-Gaussian quantum fluctuations in neutrino entanglement, *Phys. Rev. D* **106**, 123006 (2022).
- [34] R. Bhaskar, A. Roggero, and M. J. Savage, Timescales in many-body fast-neutrino-flavor conversion, *Phys. Rev. C* **110**, 045801 (2024).
- [35] J. D. Martin, D. Neill, A. Roggero, H. Duan, and J. Carlson, Equilibration of quantum many-body fast neutrino flavor oscillations, *Phys. Rev. D* **108**, 123010 (2023).
- [36] J. D. Martin, A. Roggero, H. Duan, and J. Carlson, Many-body neutrino flavor entanglement in a simple dynamic model, [arXiv:2301.07049](https://arxiv.org/abs/2301.07049) [hep-ph] (2023).
- [37] D. Lacroix, A. Bauge, B. Yilmaz, M. Mangin-Brinet, A. Roggero, and A. B. Balantekin, Phase-space methods for neutrino oscillations: Extension to multibeams,

- Phys. Rev. D* **110**, 103027 (2024).
- [38] S. Shalgar and I. Tamborra, Do we have enough evidence to invalidate the mean-field approximation adopted to model collective neutrino oscillations?, *Phys. Rev. D* **107**, 123004 (2023).
- [39] A. Kost, L. Johns, and H. Duan, Once-in-a-lifetime encounter models for neutrino media: From coherent oscillations to flavor equilibration, *Phys. Rev. D* **109**, 103037 (2024).
- [40] L. Johns, Neutrino many-body correlations, [arXiv:2305.04916 \[hep-ph\]](https://arxiv.org/abs/2305.04916) (2023).
- [41] V. Cirigliano, S. Sen, and Y. Yamauchi, Neutrino many-body flavor evolution: The full hamiltonian, *Phys. Rev. D* **110**, 123028 (2024).
- [42] M. Goimil-García, S. Shalgar, and I. Tamborra, Pauli blocking: probing beyond-mean-field effects in neutrino flavor evolution, [arXiv:2412.12268 \[astro-ph.HE\]](https://arxiv.org/abs/2412.12268) (2024).
- [43] Y. Pehlivan, A. B. Balantekin, and T. Kajino, Neutrino Magnetic Moment, CP Violation and Flavor Oscillations in Matter, *Phys. Rev. D* **90**, 065011 (2014).
- [44] P. Siwach, A. M. Suliga, and A. B. Balantekin, Entanglement in three-flavor collective neutrino oscillations, *Phys. Rev. D* **107**, 023019 (2023).
- [45] I. Chernyshev, C. E. P. Robin, and M. J. Savage, *Quantum magic and computational complexity in the neutrino sector* (2024), [arXiv:2411.04203 \[quant-ph\]](https://arxiv.org/abs/2411.04203).
- [46] N. Klco, A. Roggero, and M. J. Savage, Standard model physics and the digital quantum revolution: thoughts about the interface, *Reports on Progress in Physics* **85**, 064301 (2022).
- [47] C. W. Bauer *et al.*, Quantum Simulation for High-Energy Physics, *PRX Quantum* **4**, 027001 (2023).
- [48] A. Di Meglio *et al.*, Quantum computing for high-energy physics: State of the art and challenges, *PRX Quantum* **5**, 037001 (2024).
- [49] B. Hall, A. Roggero, A. Baroni, and J. Carlson, Simulation of collective neutrino oscillations on a quantum computer, *Phys. Rev. D* **104**, 063009 (2021).
- [50] K. Yeter-Aydeniz, S. Bangar, G. Siopsis, and R. C. Pooser, Collective neutrino oscillations on a quantum computer, *Quant. Inf. Proc.* **21**, 84 (2022).
- [51] M. Illa and M. J. Savage, Basic elements for simulations of standard-model physics with quantum annealers: Multigrid and clock states, *Phys. Rev. A* **106**, 052605 (2022).
- [52] V. Amitrano, A. Roggero, P. Luchi, F. Turro, L. Vespucci, and F. Pederiva, Trapped-ion quantum simulation of collective neutrino oscillations, *Phys. Rev. D* **107**, 023007 (2023).
- [53] M. Illa and M. J. Savage, Multi-neutrino entanglement and correlations in dense neutrino systems, *Phys. Rev. Lett.* **130**, 221003 (2023).
- [54] P. Siwach, K. Harrison, and A. B. Balantekin, Collective neutrino oscillations on a quantum computer with hybrid quantum-classical algorithm, *Phys. Rev. D* **108**, 083039 (2023).
- [55] F. Turro, I. A. Chernyshev, R. Bhaskar, and M. Illa, *Qutrit and qubit circuits for three-flavor collective neutrino oscillations* (2025), [arXiv:2407.13914 \[quant-ph\]](https://arxiv.org/abs/2407.13914).
- [56] I. A. Chernyshev, Three-flavor collective neutrino oscillation simulations on a qubit quantum annealer, *Phys. Rev. D* **111**, 043017 (2025).
- [57] A. M. Childs, Y. Su, M. C. Tran, N. Wiebe, and S. Zhu, Theory of trotter error with commutator scaling, *Phys. Rev. X* **11**, 011020 (2021).
- [58] M. J. Molewski and B. J. P. Jones, Scalable qubit representations of neutrino mixing matrices, *Phys. Rev. D* **105**, 056024 (2022).
- [59] Y. Wang, Z. Hu, B. C. Sanders, and S. Kais, Qudits and high-dimensional quantum computing, *Frontiers in Physics* **8**, 10.3389/fphy.2020.589504 (2020).
- [60] A. Morvan, V. V. Ramasesh, M. S. Blok, J. M. Kreikebaum, K. O'Brien, L. Chen, B. K. Mitchell, R. K. Naik, D. I. Santiago, and I. Siddiqi, Qutrit randomized benchmarking, *Phys. Rev. Lett.* **126**, 210504 (2021).
- [61] H. de Guise, O. Di Matteo, and L. L. Sánchez-Soto, Simple factorization of unitary transformations, *Phys. Rev. A* **97**, 022328 (2018).
- [62] N. Goss, A. Morvan, B. Marinelli, B. K. Mitchell, L. B. Nguyen, R. K. Naik, L. Chen, C. Jünger, J. M. Kreikebaum, D. I. Santiago, J. J. Wallman, and I. Siddiqi, High-fidelity qutrit entangling gates for superconducting circuits, *Nature Communications* **13**, 7481 (2022).
- [63] L. B. Nguyen, N. Goss, K. Siva, Y. Kim, E. Younis, B. Qing, A. Hashim, D. I. Santiago, and I. Siddiqi, Empowering a qudit-based quantum processor by traversing the dual bosonic ladder, *Nature Communications* **15**, 7117 (2024).
- [64] M. S. Blok, V. V. Ramasesh, T. Schuster, K. O'Brien, J. M. Kreikebaum, D. Dahlen, A. Morvan, B. Yoshida, N. Y. Yao, and I. Siddiqi, Quantum information scrambling on a superconducting qutrit processor, *Phys. Rev. X* **11**, 021010 (2021).
- [65] M. Urbanek, B. Nachman, V. R. Pascuzzi, A. He, C. W. Bauer, and W. A. de Jong, Mitigating depolarizing noise on quantum computers with noise-estimation circuits, *Phys. Rev. Lett.* **127**, 270502 (2021).
- [66] S. A. Rahman, R. Lewis, E. Mendicelli, and S. Powell, Self-mitigating trotter circuits for su(2) lattice gauge theory on a quantum computer, *Phys. Rev. D* **106**, 074502 (2022).
- [67] R. C. Farrell, M. Illa, A. N. Ciavarella, and M. J. Savage, Scalable circuits for preparing ground states on digital quantum computers: The schwinger model vacuum on 100 qubits, *PRX Quantum* **5**, 020315 (2024).
- [68] O. Kiss, M. Grossi, and A. Roggero, Quantum error mitigation for fourier moment computation, *Phys. Rev. D* **111**, 034504 (2025).
- [69] A. Hashim, R. K. Naik, A. Morvan, J.-L. Ville, B. Mitchell, J. M. Kreikebaum, M. Davis, E. Smith, C. Iancu, K. P. O'Brien, I. Hincks, J. J. Wallman, J. Emerson, and I. Siddiqi, Randomized compiling for scalable quantum computing on a noisy superconducting quantum processor, *Phys. Rev. X* **11**, 041039 (2021).
- [70] N. Goss, S. Ferracin, A. Hashim, A. Carignan-Dugas, J. M. Kreikebaum, R. K. Naik, D. I. Santiago, and I. Siddiqi, Extending the computational reach of a superconducting qutrit processor, *npj Quantum Information* **10**, 101 (2024).
- [71] K. J. Sung, M. J. Rančić, O. T. Lanes, and N. T. Bronn, Simulating majorana zero modes on a noisy quantum processor, *Quantum Science and Technology* **8**, 025010 (2023).
- [72] T. F. Stetina, A. Ciavarella, X. Li, and N. Wiebe, Simulating Effective QED on Quantum Computers, *Quantum* **6**, 622 (2022).
- [73] R. C. Farrell, I. A. Chernyshev, S. J. M. Powell, N. A. Zemel'skiy, M. Illa, and M. J. Savage, Preparations for

quantum simulations of quantum chromodynamics in $1+1$ dimensions. i. axial gauge, [Phys. Rev. D **107**, 054512 \(2023\)](#).

Appendix A: Hamiltonian derivation

In Sec. II, we outlined the contents of our model Hamiltonian for three-flavor neutrino oscillations. Here, we expand on its derivation, first for the vacuum oscillations (one-body) term in Appendix A 1 and then for the neutrino interactions (two-body) term in Appendix A 2.

1. Vacuum part

We obtain the term describing neutrino oscillations in vacuum from

$$\begin{aligned} H_\nu &= \sum_{q=1}^N \sum_{i=1}^3 \sqrt{p_q^2 + m_i^2} T_{ii}^q \\ &\approx \sum_{q=1}^N \sum_{i=1}^3 \left(p_q + \frac{m_i^2}{2p_q} \right) T_{ii}^q, \end{aligned} \quad (\text{A1})$$

where in the second step we used the ultra-relativistic limit. The T_{ij}^q operators are defined as

$$T_{ij}^q = \left(\bigotimes_{r=1}^{q-1} \mathbb{1}^{(r)} \right) \otimes t_{ij}^{(q)} \otimes \left(\bigotimes_{r=q+1}^N \mathbb{1}^{(r)} \right), \quad (\text{A2})$$

where $\mathbb{1}$ is the 3×3 identity matrix, while t_{ij} are 3×3 matrices with the $(i, j)^{\text{th}}$ element set to one and all others set to 0. The parenthetical index in each superscript denotes the subspace of the individual neutrino in which that particular operator resides. Thus, the index q in the superscript indicates that this composite operator acts non-trivially only on the q^{th} neutrino. The nine t_{ij} matrices can be expressed as linear combinations of nine orthonormal matrices, like the eight Gell-Mann matrices $\{\lambda_k\}_{k=1,\dots,8}$ plus the suitably normalized identity matrix $\lambda_0 = \sqrt{2/3}\mathbb{1}$. Using the completeness relation

$$\sum_{k=0}^8 [\lambda_k]_{\alpha\beta} [\lambda_k]_{\gamma\delta} = 2\delta_{\alpha\delta} \delta_{\beta\gamma}, \quad (\text{A3})$$

where $[M]_{\alpha\beta}$ denotes the $(\alpha, \beta)^{\text{th}}$ element of a matrix M , one can easily find that

$$\begin{aligned} 2[t_{ij}]_{\alpha\beta} &= \sum_{\gamma,\delta=1}^3 \sum_{k=0}^8 [\lambda_k]_{\alpha\beta} [\lambda_k]_{\gamma\delta} [t_{ij}]_{\delta\gamma} \\ &= \sum_{k=0}^8 [\lambda_k]_{\alpha\beta} \text{Tr} [\lambda_k t_{ij}]. \end{aligned} \quad (\text{A4})$$

Suppressing the explicit notation of the matrix indices, we have

$$t_{ij} = \frac{1}{3} \delta_{ij} \mathbb{1} + \frac{1}{2} \sum_{k=1}^8 [\lambda_k]_{ji} \lambda_k. \quad (\text{A5})$$

Using the results above, together with the fact that the Gell-Mann matrices are traceless, one finds $\sum_{i=1}^3 T_{ii}^k = \mathbb{1}$ for any k .

Returning to the one-body Hamiltonian, we can separate out a piece proportional to the identity as

$$H_\nu = \sum_{q=1}^N \left(p_q + \sum_{i=1}^3 \frac{m_i^2}{6p_q} \right) \mathbb{1} + \sum_{q=1}^N \sum_{i=1}^3 \left(\sum_{j \neq i} \frac{m_i^2 - m_j^2}{6p_q} \right) T_{ii}^q. \quad (\text{A6})$$

From Eq. (A5) we see the diagonal operators take the form

$$\begin{aligned} T_{11}^q &= \frac{\lambda_3^q}{2} + \frac{\lambda_8^q}{2\sqrt{3}} + \frac{1}{3} \mathbb{1}, \quad T_{22}^q = -\frac{\lambda_3^q}{2} + \frac{\lambda_8^q}{2\sqrt{3}} + \frac{1}{3} \mathbb{1}, \\ T_{33}^q &= -\frac{\lambda_8^q}{\sqrt{3}} + \frac{1}{3} \mathbb{1}, \end{aligned} \quad (\text{A7})$$

where the upper index q on the Gell-Mann matrices indicates the relevant neutrino subspace as in Eq. (A2). The final expression for the vacuum term is,

$$\begin{aligned} H_\nu &= \sum_{q=1}^N \left(p_q + \sum_{i=1}^3 \frac{m_i^2}{6p_q} \right) \mathbb{1} + \sum_{q=1}^N \frac{\Delta_{12}}{4p_q} \lambda_3^q \\ &\quad + \sum_{q=1}^N \frac{\Delta_{13} + \Delta_{23}}{4\sqrt{3}p_q} \lambda_8^q, \end{aligned} \quad (\text{A8})$$

where we introduced the squared mass splitting $\Delta_{ij}^2 = m_i^2 - m_j^2$ for convenience. Using a more compact notation and removing the irrelevant piece proportional to the identity we find

$$H_\nu = \sum_{q=1}^N \omega_q \vec{B} \cdot \vec{\lambda}_q, \quad \omega_q = \frac{\sqrt{\Delta_{12}^2 + (\Delta_{13} + \Delta_{23})^2/3}}{4p_q}. \quad (\text{A9})$$

The vector $\vec{\lambda}_q$ is an eight component vector containing the Gell-Mann matrices acting on the q^{th} neutrino, and

$$\begin{aligned} \vec{B} &= B_3 \vec{e}_3 + B_8 \vec{e}_8, \\ B_3 &= \frac{\Delta_{12}^2}{\sqrt{\Delta_{12}^2 + (\Delta_{13} + \Delta_{23})^2/3}}, \\ B_8 &= \frac{\Delta_{13} + \Delta_{23}}{\sqrt{3\Delta_{12}^2 + (\Delta_{13} + \Delta_{23})^2}}. \end{aligned} \quad (\text{A10})$$

We denote by \vec{e}_i the elementary vectors with components $\vec{e}_i^{(j)} = \delta_i^j$.

2. Neutrino-neutrino interaction

Using the same notation as the previous subsection, the forward scattering neutrino-neutrino interaction can be written as

$$H_{\nu\nu} = \frac{G_F}{\sqrt{2}V} \sum_{q \neq k} (1 - \cos(\theta_{qk})) \sum_{i,j=1}^3 T_{ij}^q T_{ji}^k, \quad (\text{A11})$$

where the coupling depends on the direction of the neutrino momenta through

$$\cos(\theta_{qk}) = \frac{\vec{p}_q \cdot \vec{p}_k}{p_q p_k}. \quad (\text{A12})$$

Using the fact that the Gell-Mann matrices are traceless and that $\text{Tr}[\lambda_m \lambda_n] = 2\delta_{mn}$ one finds

$$\sum_{i,j=1}^3 T_{ij}^q T_{ji}^k = \frac{1}{3} \mathbb{1} + \frac{1}{2} \vec{\lambda}_q \cdot \vec{\lambda}_k. \quad (\text{A13})$$

Removing the inconsequential part proportional to the identity, the full interaction Hamiltonian takes the form

$$\begin{aligned} H_{\nu\nu} &= \frac{G_F}{2\sqrt{2}V} \sum_{q \neq k} (1 - \cos(\theta_{qk})) \vec{\lambda}_q \cdot \vec{\lambda}_k \\ &= \frac{\mu}{4N} \sum_{q \neq k} (1 - \cos(\theta_{qk})) \vec{\lambda}_q \cdot \vec{\lambda}_k, \end{aligned} \quad (\text{A14})$$

where in the second equality we introduced the coupling constant $\mu = \sqrt{2}G_F n_\nu$, where n_ν is the neutrino density.

Appendix B: Trotter Error

In Sec. III, we cite upper bounds on the error associated with Trotterizing our time evolution operator in terms of the coupling strength, oscillation frequencies, and system size. Below we elaborate on how these bounds are obtained, considering separately commutators between two-body terms and those between two- and one-body terms of our Hamiltonian.

The commutator between the one- and two-body terms is,

$$\begin{aligned} C_{12} = [H_\nu, H_{\nu\nu}] &= \sum_{j=1}^N \sum_{q < k}^N J_{qk} \omega_j [\vec{B} \cdot \vec{\lambda}_j, \vec{\lambda}_q \cdot \vec{\lambda}_k] \\ &= \sum_{q < k}^N J_{qk} [\omega_k \vec{B} \cdot \vec{\lambda}_k + \omega_q \vec{B} \cdot \vec{\lambda}_q, \vec{\lambda}_q \cdot \vec{\lambda}_k] \end{aligned} \quad (\text{B1})$$

where Gell-Mann matrices acting on different neutrinos

commute. Since \vec{B} has only two non-zero components,

$$[\vec{B} \cdot \vec{\lambda}_k, \vec{\lambda}_q \cdot \vec{\lambda}_k] = B_3 [\lambda_3^k, \vec{\lambda}_q \cdot \vec{\lambda}_k] + B_8 [\lambda_8^k, \vec{\lambda}_q \cdot \vec{\lambda}_k]. \quad (\text{B2})$$

One can easily verify that

$$\|[\lambda_3^k, \vec{\lambda}_q \cdot \vec{\lambda}_k]\| = 4 \quad \|[\lambda_8^k, \vec{\lambda}_q \cdot \vec{\lambda}_k]\| = 2\sqrt{3}. \quad (\text{B3})$$

Additionally,

$$[\vec{B} \cdot \vec{\lambda}_k, \vec{\lambda}_q \cdot \vec{\lambda}_k] = -[\vec{B} \cdot \vec{\lambda}_q, \vec{\lambda}_q \cdot \vec{\lambda}_k]. \quad (\text{B4})$$

Then, the norm of the commutator is,

$$\begin{aligned} \|C_{12}\| &\leq \sum_{q < k}^N J_{qk} \|[\omega_k \vec{B} \cdot \vec{\lambda}_k + \omega_q \vec{B} \cdot \vec{\lambda}_q, \vec{\lambda}_q \cdot \vec{\lambda}_k]\| \\ &= \sum_{q < k}^N J_{qk} \|(\omega_k - \omega_q) [\vec{B} \cdot \vec{\lambda}_k, \vec{\lambda}_q \cdot \vec{\lambda}_k]\| \\ &= \sum_{q < k}^N J_{qk} |\omega_k - \omega_q| \|[\vec{B} \cdot \vec{\lambda}_k, \vec{\lambda}_q \cdot \vec{\lambda}_k]\| \\ &\leq (4B_3 + 2\sqrt{3}B_8) \sum_{q < k}^N J_{qk} |\omega_k - \omega_q| \\ &= \frac{4\Delta_{12}^2 + 2(\Delta_{13}^2 + \Delta_{23}^2)}{\sqrt{\Delta_{12}^4 + (\Delta_{13}^2 + \Delta_{23}^2)^2/3}} \sum_{q < k}^N J_{qk} |\omega_k - \omega_q|. \end{aligned} \quad (\text{B5})$$

We can find a simpler, though less strict, upper bound by using

$$J_{qk} \leq \frac{\mu}{N} \quad \Delta_{12}^2 < 0.1 \max[\Delta_{23}^2, \Delta_{13}^2], \quad (\text{B6})$$

to write

$$\|C_{12}\| < 4 \frac{2\mu}{2N} \binom{N}{2} \max_{q,k} |\omega_k - \omega_q| < 2\mu N \max_{q,k} |\omega_k - \omega_q|. \quad (\text{B7})$$

We now consider the purely two-body commutators' size:

$$C_{22} = \sum_{K=1}^{\binom{N}{2}} J_K \left\| \left[\vec{\lambda}_{q_K} \cdot \vec{\lambda}_{k_K}, \sum_{L > K} \vec{\lambda}_{q_L} \cdot \vec{\lambda}_{k_L} \right] \right\| \quad (\text{B8})$$

where J_K is the coupling strength for the pair $K = 1, \dots, \binom{N}{2}$. The five types of contributions that result in nontrivial the commutators are the following (see also the two flavor derivation in Ref. [52] for more details)

- $q_L < q_K$ and $k_L = q_K > q_L$
- $q_L < q_K$ and $k_L = k_K > q_L$
- $q_L = q_K$ and $k_L \neq k_K$ and $k_L > q_L$
- $k_K > q_L > q_K$ and $k_L = k_K > q_L$
- $q_L = k_K$ and $k_L > q_L$

We can therefore rewrite the sum of commutators as follows

$$\begin{aligned}
& \sum_{q < k}^N J_{qk} \left\| \left[\vec{\lambda}_q \cdot \vec{\lambda}_k, \sum_{l=1}^{q-1} J_{lq} \vec{\lambda}_l \cdot \vec{\lambda}_q + \sum_{l=1}^{q-1} J_{lk} \vec{\lambda}_l \cdot \vec{\lambda}_k + \sum_{l=q+1}^{k-1} J_{lq} \vec{\lambda}_q \cdot \vec{\lambda}_l + \sum_{l=k+1}^N J_{lq} \vec{\lambda}_q \cdot \vec{\lambda}_l + \sum_{l=q+1}^{k-1} J_{lk} \vec{\lambda}_l \cdot \vec{\lambda}_k + \sum_{l=k+1}^N J_{lk} \vec{\lambda}_k \cdot \vec{\lambda}_l \right] \right\| \\
&= \sum_{q < k}^N J_{qk} \left\| \left[\vec{\lambda}_q \cdot \vec{\lambda}_k, \sum_{l=1}^{q-1} \vec{\lambda}_l \cdot (J_{lq} \vec{\lambda}_q + J_{lk} \vec{\lambda}_k) + \sum_{l=q+1}^{k-1} \vec{\lambda}_l \cdot (J_{lq} \vec{\lambda}_q + J_{lk} \vec{\lambda}_k) + \sum_{l=k+1}^N \vec{\lambda}_l \cdot (J_{lq} \vec{\lambda}_q + J_{lk} \vec{\lambda}_k) \right] \right\|
\end{aligned} \tag{B9}$$

At this point we need the commutator identity

$$\begin{aligned}
[\vec{\lambda}_q \cdot \vec{\lambda}_k, \vec{\lambda}_q \cdot \vec{\lambda}_l] &= \sum_{n=1}^8 \sum_{m=1}^8 [\lambda_m^q, \lambda_n^q] \lambda_m^k \lambda_n^l \\
&= 2i \sum_{n=1}^8 \sum_{m=1}^8 \sum_{j=1}^8 f^{m n j} \lambda_j^q \lambda_m^k \lambda_n^l \tag{B10} \\
&= \sum_{n < m}^8 [\lambda_m^q, \lambda_n^q] (\lambda_m^k \lambda_n^l - \lambda_n^k \lambda_m^l)
\end{aligned}$$

From the last result in the second line it is clear using the anti-symmetry of the structure constants that

$$[\vec{\lambda}_q \cdot \vec{\lambda}_k, \vec{\lambda}_k \cdot \vec{\lambda}_l] = - [\vec{\lambda}_q \cdot \vec{\lambda}_k, \vec{\lambda}_q \cdot \vec{\lambda}_l]. \tag{B11}$$

A direct calculations then shows that

$$\left\| [\vec{\lambda}_q \cdot \vec{\lambda}_k, \vec{\lambda}_q \cdot \vec{\lambda}_l] \right\| = 4\sqrt{3}. \tag{B12}$$

Using these results we can then find the upper bound

$$\begin{aligned}
\|C_{22}\| &\leq 4\sqrt{3} \sum_{q < k}^N J_{qk} \left(\sum_{l=1}^{q-1} |J_{lq} - J_{lk}| \right. \\
&\quad \left. + \sum_{l=q+1}^{k-1} |J_{lq} - J_{lk}| \right. \\
&\quad \left. + \sum_{l=k+1}^N |J_{lq} - J_{lk}| \right) \tag{B13} \\
&< 4\sqrt{3} \sum_{q < k}^N J_{qk} \sum_{l=1}^N |J_{lq} - J_{lk}|.
\end{aligned}$$

As we did before, we can find simpler bounds by bound-

ing the J_{qk} coupling constants

$$\begin{aligned}
\|C_{22}\| &< 4\sqrt{3} \frac{2\mu}{2N} \frac{\mu}{2N} \binom{N}{2} \sum_{l=1}^N \max_{q,k} |\cos(\theta_{lq}) - \cos(\theta_{lk})| \\
&< \sqrt{3} \mu^2 \sum_{l=1}^N \max_{q,k} |\cos(\theta_{lq}) - \cos(\theta_{lk})|
\end{aligned} \tag{B14}$$

or the even simpler one

$$\|C_{22}\| < \sqrt{3} \mu^2 N \max_{q,k,l} |\cos(\theta_{lq}) - \cos(\theta_{lk})|. \tag{B15}$$

We can now put everything together and get an error bound for a first-order Trotter decomposition. We proceed in two steps by first splitting the one and two body evolution obtaining [52, 57]

$$\|e^{-iHt} - e^{-itH_\nu} e^{-itH_{\nu\nu}}\| \leq \frac{t^2}{2} \|C_{12}\|. \tag{B16}$$

We then split the two body evolution into a product of evolutions over individual pairs as follows

$$U_{pair}(t) = \prod_{q < k} e^{-itJ_{qk} \vec{\lambda}_q \cdot \vec{\lambda}_k}. \tag{B17}$$

The errors we incur by doing this is

$$\|e^{-itH_{\nu\nu}} - U_{pair}(t)\| \leq \frac{t^2}{2} \|C_{22}\|. \tag{B18}$$

Putting all together by doing r steps of size t/r each we finally have

$$\begin{aligned}
\left\| e^{-iHt} - \prod_{s=1}^r e^{-i\frac{t}{r}H_\nu} U_{pair} \left(\frac{t}{r} \right) \right\| &\leq r \left\| e^{-iH\frac{t}{r}} - e^{-i\frac{t}{r}H_\nu} U_{pair} \left(\frac{t}{r} \right) \right\| \\
&\leq r \left\| e^{-iH\frac{t}{r}} - e^{-i\frac{t}{r}H_\nu} e^{-i\frac{t}{r}H_{\nu\nu}} \right\| + r \left\| e^{-i\frac{t}{r}H_\nu} e^{-i\frac{t}{r}H_{\nu\nu}} - e^{-i\frac{t}{r}H_\nu} U_{pair} \left(\frac{t}{r} \right) \right\| \\
&\leq \frac{t^2}{2r} (\|C_{12}\| + \|C_{22}\|) \\
&< \frac{t^2}{2r} \mu N \left(2 \max_{q,k} |\omega_k - \omega_q| + \sqrt{3} \mu \max_{q,k,l} |\cos(\theta_{lq}) - \cos(\theta_{lk})| \right)
\end{aligned} \tag{B19}$$

If we use the short hand notation

$$\Delta\omega_{max} = \max_{q,k} |\omega_k - \omega_q| \tag{B20}$$

$$\Delta\theta_{max} = \max_{q,k,l} |\cos(\theta_{lq}) - \cos(\theta_{lk})|. \tag{B21}$$

We have that the total number of steps to guarantee an error ϵ over a total time evolution interval of size t is

$$\begin{aligned}
r &= \frac{t^2}{2\epsilon} \mu N \left(2\Delta\omega_{max} + \sqrt{3}\mu\Delta\theta_{max} \right) \\
&= \mathcal{O} \left(\frac{t^2 \mu N}{\epsilon} (\Delta\omega_{max} + \mu) \right).
\end{aligned} \tag{B22}$$

By using the same strategy used in Ref. [52] to bound the error of the second-order formula with two flavors, we can extend this result and show a scaling linear in system size N for all the higher order Trotter formulas.

Appendix C: Qubit quantum circuit

In Sec. VA, we outline our procedure to simulate three-flavor collective oscillations on qubit-based hardware. Here, we derive the circuits to perform these simulations in terms of elementary gates in the following order: First, we explore in Appendix C1 how to transform from the flavor basis, in which we prepare our initial wave function and measure our evolved state, and the mass basis where time evolution will be performed. To follow up, we show how to decompose exponentials of one- and two-body terms in the Hamiltonian into elementary gates in Appendices C2 and C3, respectively, allowing us to perform time steps with the desired Hamiltonian model. These decompositions involve a number of useful algebraic identities that we prove in Appendix C4.

1. PMNS matrix

The unitary operator mixing neutrino flavor and mass eigenstates is the PMNS matrix:

$$\begin{pmatrix} \nu_e \\ \nu_\mu \\ \nu_\tau \end{pmatrix} = U_{\text{PMNS}} \times \begin{pmatrix} \nu_1 \\ \nu_2 \\ \nu_3 \end{pmatrix}, \tag{C1}$$

$$\begin{aligned}
U_{\text{PMNS}} &= \begin{bmatrix} 1 & 0 & 0 \\ 0 & c_{23} & s_{23} \\ 0 & -s_{23} & c_{23} \end{bmatrix} \times \begin{bmatrix} c_{13} & 0 & s_{13}e^{-i\delta_{\text{CP}}} \\ 0 & 1 & 0 \\ -s_{13}e^{i\delta_{\text{CP}}} & 0 & c_{13} \end{bmatrix} \\
&\times \begin{bmatrix} c_{12} & s_{12} & 0 \\ -s_{12} & c_{12} & 0 \\ 0 & 0 & 1 \end{bmatrix}
\end{aligned} \tag{C2}$$

where $c_{ij} := \cos(\theta_{ij})$, $s_{ij} := \sin(\theta_{ij})$. Since we are using a qubit mapping where the $|00\rangle$ state is non-physical, we can write the three rotation matrices as follows:

$$\begin{pmatrix} 1 & 0 & 0 & 0 \\ 0 & 1 & 0 & 0 \\ 0 & 0 & c_{23} & s_{23} \\ 0 & 0 & -s_{23} & c_{23} \end{pmatrix} = \begin{array}{c} \bullet \\ | \\ \text{---} R_y(-2\theta_{23}) \text{---} \\ | \\ \oplus \end{array} \tag{C3}$$

$$\begin{pmatrix} 1 & 0 & 0 & 0 \\ 0 & c_{13} & 0 & s_{13} \\ 0 & 0 & 1 & 0 \\ 0 & -s_{13} & 0 & c_{13} \end{pmatrix} = \begin{array}{c} \text{---} R_y(-2\theta_{23}) \text{---} \\ | \\ \bullet \end{array} \tag{C4}$$

and the Givens rotation from Ref. [71]

$$\begin{pmatrix} 1 & 0 & 0 & 0 \\ 0 & c_{12} & s_{12} & 0 \\ 0 & -s_{12} & c_{12} & 0 \\ 0 & 0 & 0 & 1 \end{pmatrix} = \begin{array}{c} \text{---} R_y(\pi/2) \text{---} \bullet \text{---} R_y(-\theta_{23}) \text{---} \bullet \text{---} R_y(-\pi/2) \text{---} \\ | \oplus \text{---} R_y(-\theta_{23}) \text{---} \oplus | \end{array} \tag{C5}$$

The inclusion of a CP phase can be accomplished easily with single-qubit Z rotations;

$$\begin{aligned}
&\begin{pmatrix} 1 & 0 & 0 & 0 \\ 0 & c_{13} & 0 & s_{13}e^{-i\delta_{\text{CP}}} \\ 0 & 0 & 1 & 0 \\ 0 & -s_{13}e^{i\delta_{\text{CP}}} & 0 & c_{13} \end{pmatrix} \\
&= \begin{array}{c} \text{---} R_z(-\delta_{\text{CP}}) \text{---} R_y(-2\theta_{23}) \text{---} R_z(\delta_{\text{CP}}) \text{---} \\ | \\ \bullet \end{array}
\end{aligned} \tag{C6}$$

Alternatively, to realize the PMNS matrix with the cross-resonance gate $R_{ZX}(\theta)$, let us introduce some relations: an arbitrary Y rotation can always be written as $R_y(\theta) = SHR_z(\theta)HS^\dagger$, while the commutation relation between S or S^\dagger and a CNOT are as follows

$$\begin{array}{c} \bullet \\ | \\ \oplus \text{---} S \text{---} \\ | \end{array} = \begin{array}{c} \text{---} S \text{---} \bullet \text{---} \bullet \text{---} \\ | \bullet \text{---} \oplus | \end{array} \tag{C7}$$

$$(C8)$$

Since we can write a controlled-rotation using two CNOTs as

$$(C9)$$

we can then write it in terms of the cross-resonance gate as:

$$(C10)$$

recalling the relation between R_{ZX} and R_{ZZ} :

$$(C11)$$

where $U_{1,1} = R_z(\pi/2)\sqrt{X}R_z(\pi/2)$ is the Hadamard gate H up to a global phase, in particular $U_{1,1} = e^{i\pi/4}H$. As for the Givens rotation instead, we find the following circuit:

$$(C12)$$

In this way, it is possible to write the PMNS matrix either with two CNOTs plus two controlled- R_Y rotations, or with four cross-resonance gates R_{ZX} .

2. One-body terms

Next, we outline how to realize the one-body terms of Eq. (1) with elementary gates acting on qubit hardware. To start, note the mass basis the one body term is, per our encoding in Sec. IV,

$$H_\nu = \sum_p \omega_p \vec{B} \cdot \vec{Q}_p = \sum_p \omega_p (B_3 Q_{3p} + B_8 Q_{8p}), \quad (C13)$$

where we can simplify the operator into

$$B_3 Q_{3p} + B_8 Q_{8p} = \left(\frac{B_3}{2} + \frac{B_8}{2\sqrt{3}} \right) (\sigma_3 \otimes \sigma_0)_p - \left(\frac{B_3}{2} - \frac{B_8}{2\sqrt{3}} \right) (\sigma_0 \otimes \sigma_3)_p - \frac{B_8}{\sqrt{3}} (\sigma_3 \otimes \sigma_3)_p \quad (C14)$$

Let us denote with labels A and B the two qubits for a given momentum mode p . The time evolution operator for a single neutrino acting on the qubit pair is,

$$U_1(t) = R_B^z \left(\omega_p t \left(B_3 + \frac{B_8}{\sqrt{3}} \right) \right) \times R_A^z \left(-\omega_p t \left(B_3 - \frac{B_8}{\sqrt{3}} \right) \right) \times R_{AB}^{zz} \left(-2\omega_p \frac{B_8}{\sqrt{3}} t \right) \quad (C15)$$

Using the fact that we are free to keep an arbitrary phase on the unphysical state $|00\rangle$, and everything is invariant up to a global phase, the evolution unitary we actually need to implement is the following simplification:

$$\tilde{U}_1(t) = R_B^z \left(\omega_p t \left(B_3 + \frac{B_8}{\sqrt{3}} \right) \right) \times R_A^z \left(-\omega_p t \left(B_3 - \frac{B_8}{\sqrt{3}} \right) \right). \quad (C16)$$

3. Two-body terms

Finally, we outline how to realize the interaction Hamiltonian of Eq. (3) on qubits, also using the representation of Sec. IV. We draw inspiration from the circuit constructions derived in Refs. [72, 73] using diagonalization gadgets. Let us introduce the diagonalizing operators G_{ab} and K defined as follows:

$$(C17)$$

$$(C18)$$

Indeed, these operators diagonalize the following terms (remember our notation $Q_i \otimes Q_i =: Q_{ii}$):

$$G_{13} (Q_{44} + Q_{55}) G_{13}^\dagger = \frac{Z_1 - Z_1 Z_3}{4} (1 - Z_4 - Z_2 + Z_2 Z_4)$$

$$K (Q_{11} + Q_{22}) K^\dagger = \frac{Z_1 - Z_1 Z_2}{4} (1 - Z_3 + Z_4 - Z_3 Z_4)$$

$$G_{24} (Q_{66} + Q_{77}) G_{24}^\dagger = \frac{Z_2 - Z_2 Z_4}{4} (1 - Z_1 - Z_3 + Z_3 Z_1) \quad (C19)$$

The proof of these equalities is shown in Appendix C4. We can then use the fact that $Gf(\vec{Q})G^\dagger = f(G\vec{Q}G^\dagger)$ for every f whose Taylor expansion is well-defined. So, from the first equality of Eq. (C19) we find that the implementation of $G_{13} e^{i\alpha(Q_4 \otimes Q_4 + Q_5 \otimes Q_5)} G_{13}^\dagger$ can be achieved with

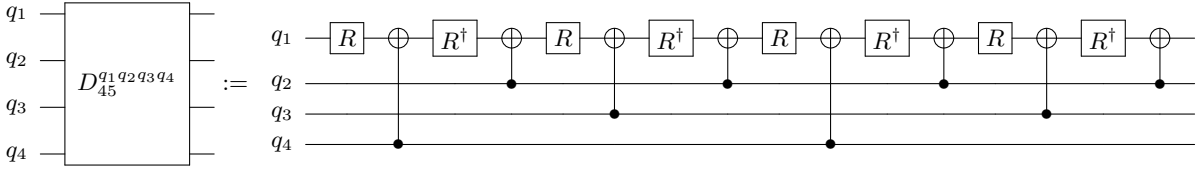


FIG. 3. Diagonal unitary required to implement $\exp(i\alpha(Q_4 \otimes Q_4 + Q_5 \otimes Q_5))$ in conjunction with the operator G_{13} from Eq. (C17). The single qubit gate R is a Z rotation with angle α

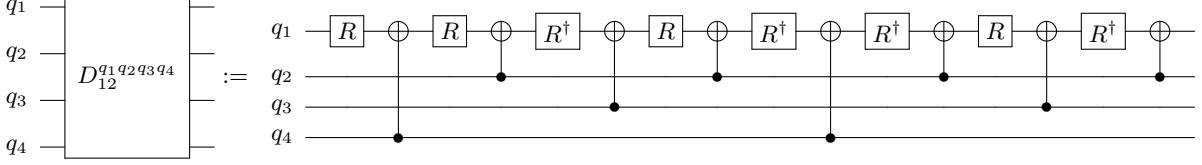


FIG. 4. Diagonal unitary required to implement $\exp(i\alpha(Q_1 \otimes Q_1 + Q_2 \otimes Q_2))$ in conjunction with the operator K from Eq. (C18). The single qubit gate R is a Z rotation with angle α .

the diagonal circuit D_{45}^{1234} (where the superscript denotes the order of qubits) shown in Fig. 3.

With a permutation of qubits $(1, 3) \rightarrow (2, 4)$ we find that $G_{24} e^{i\alpha(Q_6 \otimes Q_6 + Q_7 \otimes Q_7)} G_{24}^\dagger$ can be implemented by the same circuit, which with the notation of before would be D_{45}^{2143} . Both of these terms can be done with 10 CNOT each for all-to-all connectivity. The unitary operator corresponding to $K e^{i\alpha(Q_1 \otimes Q_1 + Q_2 \otimes Q_2)} K^\dagger$ is slightly different, and it is implemented by the circuit shown in Fig. 4. Together with the cost of implementing the unitary K , and its inverse, the cost of the full evolution for this term is 14 CNOT gates with all-to-all connectivity.

The last operation we need to perform is the evolution under the two diagonal generators:

$$Q_{33} + Q_{88} = -\frac{2}{3}\mathbb{1} + 2(Z_1 Z_3 + Z_2 Z_4 + Z_1 Z_2 Z_3 Z_4) \quad (\text{C20})$$

This expression for $Q_3 \otimes Q_3 + Q_8 \otimes Q_8$ was obtained by adding operators that only modify the unphysical Hilbert space. Since $G_{13} Z_1 Z_3 G_{13}^\dagger = Z_3$ (and the same holds for $Z_2 Z_4$ with G_{24}) we can implement this operator by simply adding a single qubit rotation when we perform the diagonal pieces D_{45} shown in Fig. 3. As for the $Z_1 Z_2 Z_3 Z_4$ term instead, we can implement it by introducing the new operator O_i , where the i index denotes the target qubit, which gives $O_i Z_1 Z_2 Z_3 Z_4 O_i = Z_i$. (Note $O^\dagger = O$.) This operation is simple to perform with three CNOT gates, for instance O_1 can be implemented as

$$O_1 = \text{CNOT}(q_1, q_2) \text{CNOT}(q_1, q_3) \text{CNOT}(q_1, q_4) \quad (\text{C21})$$

In summary, with an all-to-all connectivity, we can implement the full two-body interaction term with the circuit shown in Fig. 5. In the shown implementation we

simplified together two CNOT gates shared between G_{13} and K^\dagger reducing the gate count to 38 CNOTs. In addition, four more CNOT gates can be removed simplifying gates shared with O_4 bringing the final CNOT count to 34. We can also consider the case, like on the IBM device we employed for the simulations shown in the main text, of 4 qubits with T connectivity where we have one qubit that interacts with the other 3, but where the other 3 qubits interact only with the one in the center. In this case, we see already that the diagonal unitaries in Fig. 3 and Fig. 4 are compatible with the T connectivity provided q_1 is the central qubit. We then start with qubit 1 in the middle and swap $1 \leftrightarrow 2$ in order to perform the evolution generated by $Q_6 \otimes Q_6 + Q_7 \otimes Q_7$. By choosing $O_2 Z O_2$ for the four-qubit rotation, as shown in Fig. 6, we can then cancel two of the CNOT gates in the middle SWAP with neighboring gates resulting in a total of 39 CNOT gates. At the end of the step the order of the first and second qubits is reversed.

4. Diagonalizing-relations

$$\text{Circuit} = \text{Z} \quad (\text{C22})$$

$$\text{Circuit} = -\text{Z} \quad (\text{C23})$$

$$\text{Circuit} = \text{Z} \quad (\text{C24})$$

With those relations we can easily prove the following

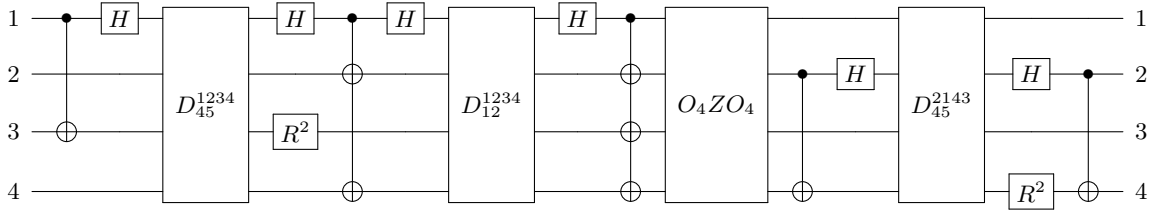


FIG. 5. Circuit implementation of the full two-body evolution operator with all-to-all connectivity.

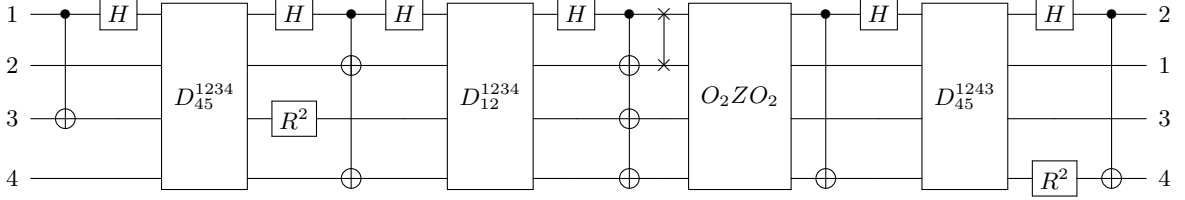


FIG. 6. Circuit implementation of the full two-body evolution operator with T connectivity.

relations:

$$G_{13}(Q_{44} + Q_{55})G_{13}^\dagger = \frac{Z_1 - Z_1 Z_3}{4} (1 - Z_4 - Z_2 + Z_2 Z_4) \quad (\text{C25})$$

$$G_{24}(Q_{66} + Q_{77})G_{24}^\dagger = \frac{Z_2 - Z_2 Z_4}{4} (1 - Z_1 - Z_3 + Z_3 Z_1) \quad (\text{C26})$$

$$\text{Circuit (C27)} = \text{Z gates on qubits 2, 3, 4} \quad (\text{C27})$$

$$\text{Circuit (C28)} = \text{-Z gates on qubits 2 and 4, Z gate on qubit 3} \quad (\text{C28})$$

$$\text{Circuit (C29)} = \text{Z gates on qubits 2 and 4, -Z gates on qubits 3 and 4} \quad (\text{C29})$$

$$\text{Circuit (C30)} = \text{Z gates on qubits 2, 3, 4} \quad (\text{C30})$$

$$\text{Circuit (C31)} = \text{Z gate on qubit 2} \quad (\text{C31})$$

With those operators we have that:

$$K(Q_1 \otimes Q_1)K^\dagger = \frac{Z_1}{4} (1 - Z_2 - Z_3 Z_4 + Z_2 Z_3 Z_4) \quad (\text{C32})$$

$$\text{Circuit (C33)} = \text{-Z gates on qubits 2 and 3, Z gate on qubit 4} \quad (\text{C33})$$

$$\text{Circuit (C34)} = \text{Z gates on qubits 2 and 4, -Z gates on qubits 3 and 4} \quad (\text{C34})$$

$$(C35)$$

$$(C36)$$

So that:

$$K(Q_2 \otimes Q_2)K^\dagger = \frac{Z_1}{4}(-Z_3 + Z_4 + Z_2Z_3 - Z_2Z_4) \quad (C37)$$

and we prove with this that the operator K diagonalizes the term $Q_1 \otimes Q_1 + Q_2 \otimes Q_2$:

$$K(Q_{11} + Q_{22})K^\dagger = \frac{Z_1 - Z_1Z_2}{4}(1 - Z_3 + Z_4 - Z_3Z_4) \quad (C38)$$

Appendix D: Complete hardware results

In this section we present the results for all states of the two neutrino systems. We start by presenting in Fig. 7 the total variation distance (TVD)

$$\delta(P_{ref}, P_{meas}) = \frac{1}{2} \sum_x |P_{ref}(x) - P_{meas}(x)|, \quad (D1)$$

between the expected distribution P_{ref} over the nine flavor states of two neutrinos and the measured distribution P_{meas} obtained from the hardware runs, with and without error mitigation. The bands are 90% confidence intervals obtained by resampling the experimental results assuming they follow a normal distribution with the estimated means and standard deviations. From these results, the beneficial effect of error mitigation is clear, consistently lowering the TVD in all cases. This analysis also shows that the qubit simulations, both with and without

error mitigation, achieve a smaller TVD than the respective calculations on qutrit hardware even though after mitigation the spread appears reduced.

In Fig. 8, data before error mitigation are shown. Each plot depicts the evolving probability of a given definite-flavor state, except the first panel which is a superposition of all other plots to underline the relative magnitude. In each case we compare qubit and qutrit with the exact result. Without any error mitigation, it is clear that hardware noise dominates our results, and data are far from the exact result after a couple of Trotter steps.

However, one difference can be found in the probabilities on hardware for states that should have a very small theoretical probability during runtime (see the plots for the $\{|\mu\mu\rangle, |\mu\tau\rangle, |\tau\mu\rangle, |\tau\tau\rangle\}$ states). The time evolution operator plays almost no role in the evolution of these states, and the major contribution is the depolarizing noise, which should converge to $1/\text{Tr}[\mathbb{1}]$ where $\text{Tr}[\mathbb{1}]$ is the total number of global states for (16 or 9 for qubits and qutrits, respectively). Since for qubits we have the presence of a nonphysical state, the depolarizing noise will converge to $1/16 \approx 0.06$. In the case of qutrits instead, the noise will converge to $1/9 \approx 0.1$. Indeed, unmitigated hardware results converge close to these values as function of time. This difference is taken into account during error mitigation, as explained in more detail in Sec. VI.

As already mentioned in Sec. VII, this distinction can give us some intuition about the impact of depolarizing noise with system scaling. Considering the qubit encoding for N neutrinos, the fraction of physical states over the total number of states is $(3/4)^N$, which vanishes as the number of neutrinos increases. Since probability amplitudes will increasingly populate unphysical states due to the depolarizing noise in the qubit case, we can expect the qutrit encoding to scale better when considering only error-mitigation strategies. In practice, the problem with unphysical state might not be so impactful if one is only interested in local, small-weight observables.

We show data after error-mitigation in Fig. 9. As before, every plot displays the probability of being in a particular final state, while the plot in the first panel shows the relative magnitude between different states. Both qubit and qutrit results are close to the exact evolution, and even information in data that looked like fully depolarized have been recovered with error mitigation. There is no clear advantage between the two methods for this small system, but scaling up the particle number should lead to the differences outlined above.

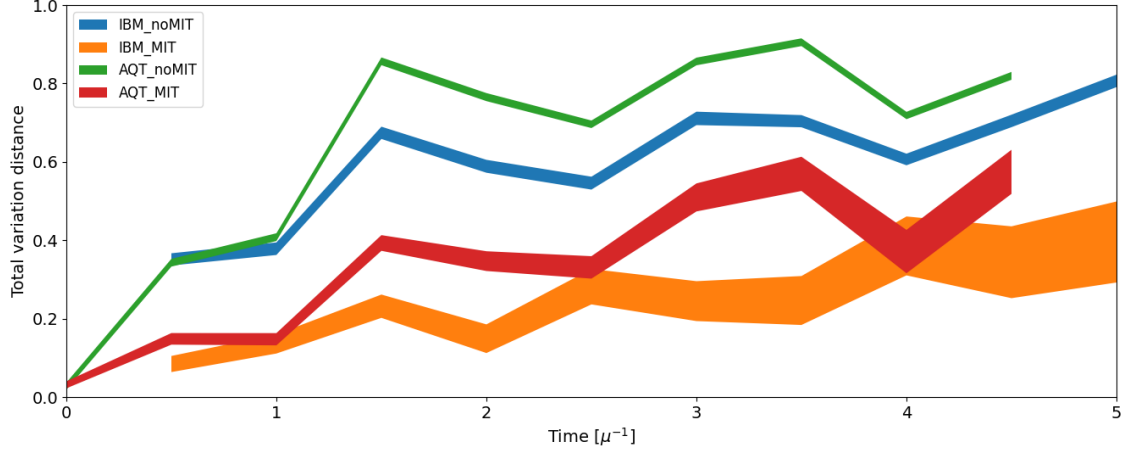


FIG. 7. Total variation distances between the expected flavor probability distribution over flavor states and the distribution estimated from quantum computations. We show in blue and orange the qubit result without (IBM_noMIT) and with (IBM_MIT) error mitigation respectively. Similarly, we report the qutrit result without error mitigation (AQT_noMIT) in green and with error mitigation (AQT_MIT) in red. The bands correspond to 90% confidence intervals.

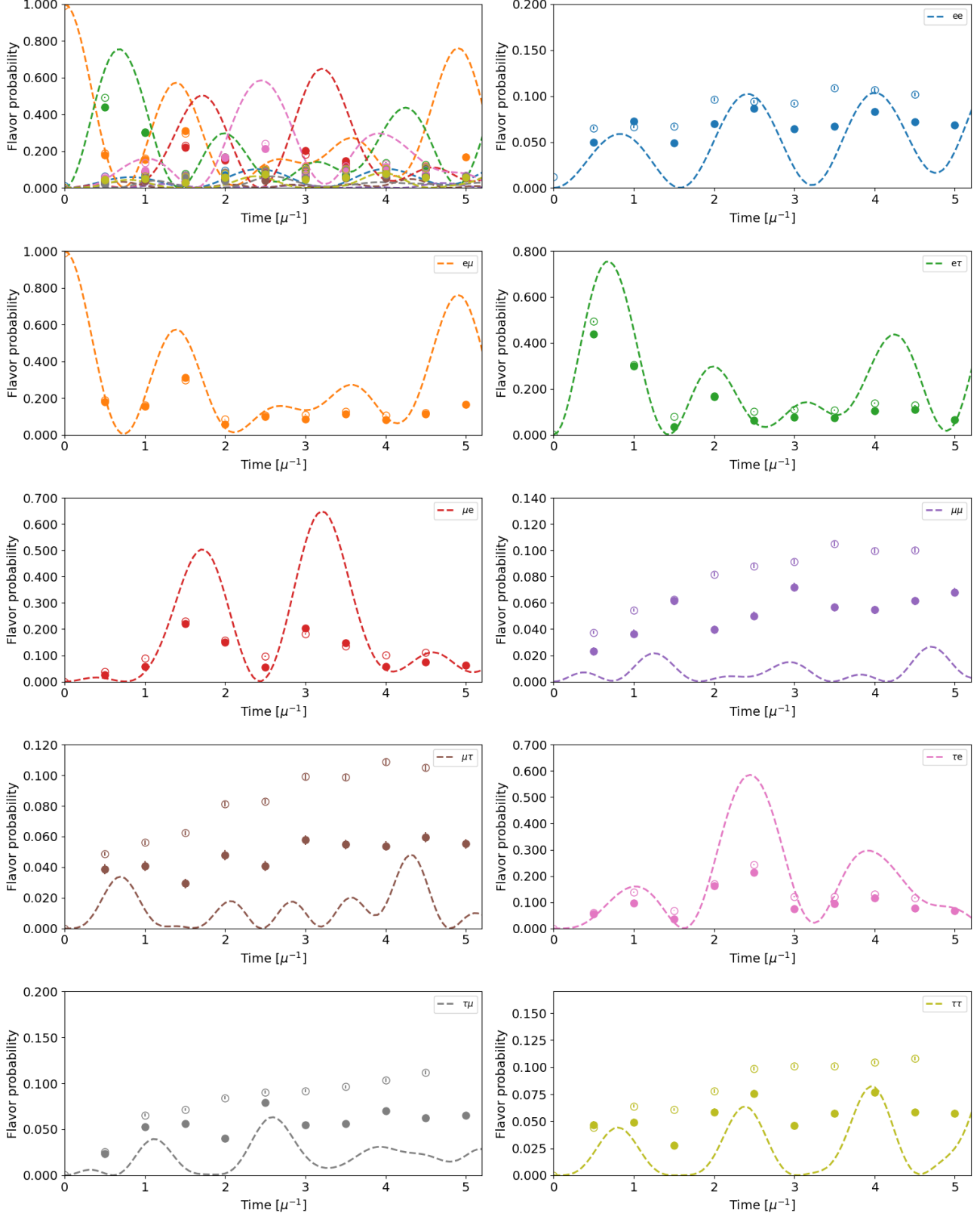


FIG. 8. The vertical axis shows the probability of occupying a given final state. We present one plot for each possible two-flavor neutrino state, while the first panel shows a summary, highlighting the relative magnitudes. We also quantify the uncertainty using standard error through the vertical error bars. The dashed line is the exact calculation, while solid and empty dots represent the qubit (IBM) and qutrit (AQT) data respectively, before error mitigation.

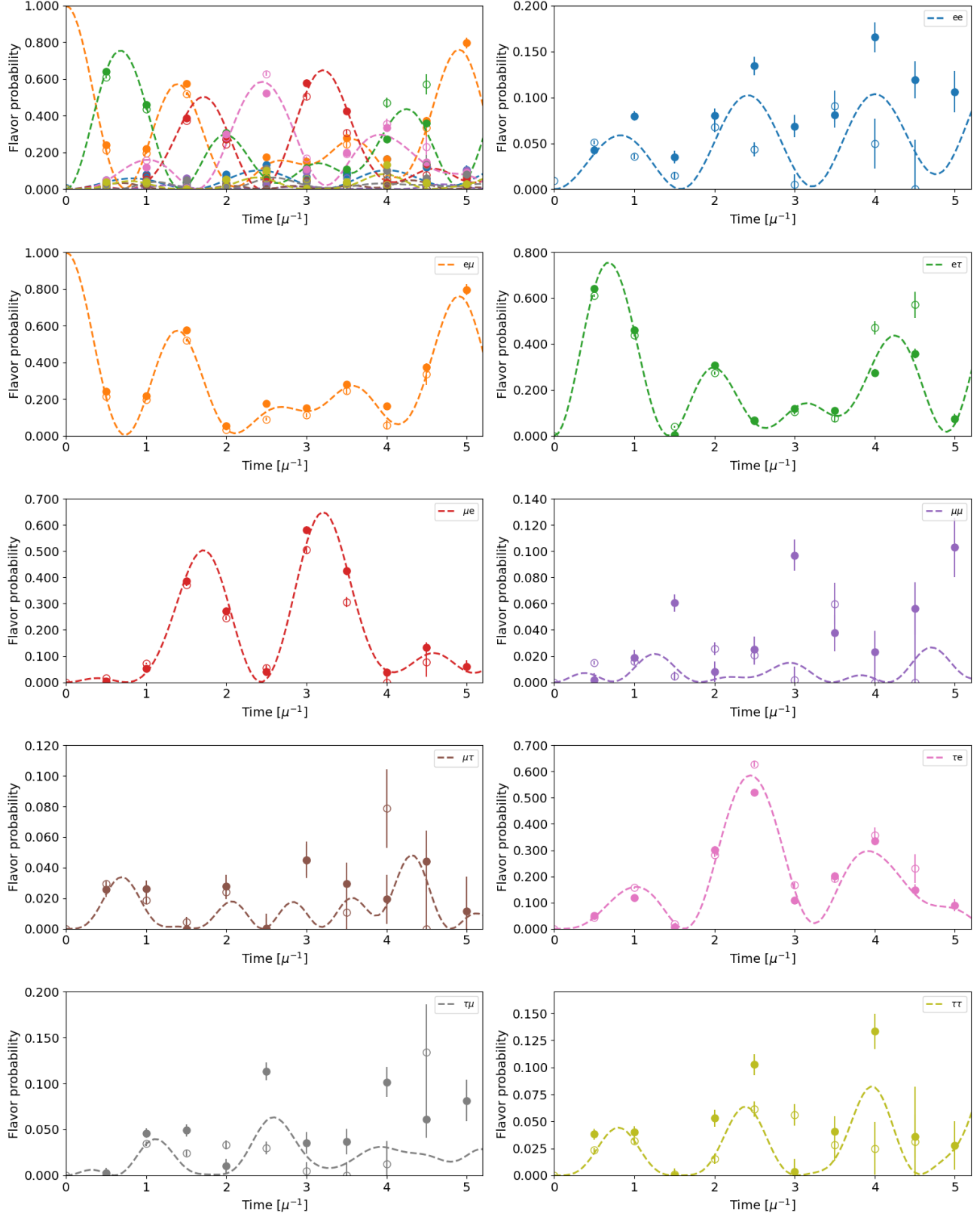


FIG. 9. The vertical axis shows the probability of occupying a given final state. We present one plot for each possible two-flavor neutrino state, while the first panel shows a summary, highlighting the relative magnitudes. The dashed line is the exact calculation, while solid and empty dots represent the qubit (IBM) and qutrit (AQT) data respectively, after error mitigation. We also quantify the uncertainty using standard error through the vertical error bars. As expected error mitigation increases the variance observed.